Revisiting the Steady States of $NO/O_2/C_3H_6$ on Monolithic $Pt/BaO/Al_2O_3$ Using Bifurcation Analysis

Wei Xu, Meng-Long Lai, Wei-Fang Yu, and Jin Xu
College of Chemistry and Materials Engineering, Wenzhou University, Chashan University Town, Wenzhou, 325035, Zhejiang, P.R. China

DOI 10.1002/aic.14263
Published online November 16, 2013 in Wiley Online Library (wileyonlinelibrary.com)

While NOx storage and reduction is periodically operated, steady-state studies have been widely carried out to investigate the involved reaction mechanisms and effects of operating parameters. Due to the complex reaction chemistry and its coupling with transport phenomena, multiplicity may exist. A steady-state monolith reactor model accounting for microkinetics and reaction heat effects was proposed in this study to avoid the evaluation of enthalpies of microreaction steps. Three simplified versions of the monolith model were developed based on various assumptions of the axial gradients. Steady-state behaviors of $NO/O_2/C_3H_6$ system were investigated. A predictor-corrector (PC) continuation method that does not require explicit evaluation of Jacobian Matrix was developed to solve the nonlinear system with a variable parameter of feed temperature. Model predictions were compared with experimental results. © 2013 American Institute of Chemical Engineers *AIChE J*, 60: 623–634, 2014

Keywords: NOx storage and reduction, catalytic monolith reactor, microkinetics, multiple steady-state, continuation method

Introduction

NOx storage and reduction (NSR) technique[1,2] has emerged as a promising alternative to meet the increasingly stringent regulations on lean-burn and diesel vehicle engines. NSR is a periodically operated process involving two alternating phases carried out in a monolithic reactor called lean NOx trap (LNT). The LNT contains a multifunctional monolithic catalyst comprising precious metals (Pt, Rh) and an alkaline-earth metal oxide (e.g., BaO) supported on a high-surface area support ($-Al_2O_3$). During the lean phase, exhaust NOx in the presence of excess oxygen is stored on the metal oxides in the form of nitrites and nitrates. Then before any significant NOx breakthrough, either the engine is run rich or a reductant is injected into the exhaust stream to produce a rich mixture for a much shorter duration than that of the storage. This rich phase serves to reduce the stored NOx and regenerate the LNT catalyst for the use of the next cycle. Experimental studies have shown that efficient NOx trapping and overall NOx conversions exceeding 90% can be obtained under cycle-averaged lean conditions.[3–5] Further optimization to achieve high NOx conversion and selectivity to N_2 with minimal fuel penalty requires a deep understanding of the catalytic chemistry and kinetics and their coupling with mass and heat-transfer processes.

During the switch between lean and rich phases, an LNT undergoes considerable changes of operating conditions in terms of temperature and feed composition.[6] In order to investigate the underlying mechanisms, complex NSR process can be divided into several simpler subnetworks, namely, NO oxidation, NOx storage and NOx reduction.[7] While NSR is a periodic process, steady-state studies have been widely carried out to probe the reaction mechanisms and kinetics, especially for NO oxidation[8–11] and NOx reduction.[12–14] NO oxidation forming NO_2 is a crucial step for efficient NOx storage[8,15] and has been extensively investigated.[8–11,16–20] Steady-state NOx reduction by H_2 and NH_3 operated under isothermal conditions were investigated in our previous studies.[13,14] This work is focused on the system of NO, O_2 and C_3H_6, a representative of hydrocarbons. Steady-state behaviors of $NO/O_2/C_3H_6$ system were previously investigated by Sharma et al.[21] both experimentally and theoretically. It was shown that multiplicity may exist in a specific range of feed temperature.[21] In this work, we revisit the system with the following updated features:

(a) The steady-state model is numerically solved using continuation method rather than by integrating the corresponding transient model to "pseudo" steady-states.

(b) Energy balance equations in the monolith reactor model are revised to avoid evaluation of surface reaction heat or enthalpies of surface species.

(c) The microkinetic model is updated according to the latest research findings and modified to avoid trivial solutions to the steady-state model.

(d) Quantitative and qualitative analyses of surface species distribution are used to explain some of the major trends.

The article is organized as follows. The steady-state monolith reactor model is first presented. Three simplified versions of the model are developed based on different descriptions of the axial gradients. Then a microkinetic model including adsorption, desorption and surface reaction steps is introduced.

Correspondence concerning this article should be addressed to W-F. Yu at ywf@wzu.edu.cn, and J. Xu at xujin@wzu.edu.cn.

Finally, temperature effects on steady-state behaviors of NO/O_2/C_3H_6 system of various feed compositions are simulated and discussed. The scheme of a simplified pseudo-arclength method that does not require explicit evaluation of Jacobian Matrix is presented in the Appendix.

Model Descriptions

Steady-state monolith reactor model

Monolith reactor model equations involved in this study were developed based on the assumptions described elsewhere.[13,14,21,22]

Component mass balance in the fluid phase

$$\overline{u_f}\frac{\partial X_{jm}}{\partial Z}+\frac{k_{jc}}{R_\Omega}\left(X_{jm}-X_{js}\right)=0 \tag{1}$$

where $\overline{u_f}$ is the average velocity, X_j is the mole fraction of component j, subscripts m and s denote to fluid and solid, respectively $k_{c,j}$ is the mass-transfer coefficient of component j, and $R$is the hydraulic radius. Mass-transfer coefficients can be calculated from $k_{c,j}=\frac{D_{jm}}{R_\Omega}Sh_\Omega$, where D_{jm} is molecular diffusivity of component j, and, for fully developed laminar flow in a circular channel, Sh_Ω equals to 1.09.[23]

Continuity of species flux between fluid and solid phase

$$C_T k_{jc}\left(X_{jm}-X_{js}\right)-\delta_c\left(R_{j,ad}-R_{j,de}\right)=0 \tag{2}$$

where C_T is the total gas phase concentration, δ_c is the wash coat thickness, $R_{j,ad}$ and $R_{j,de}$ are volumetric adsorption and desorption rates (based on wash coat volume) of component j on the catalyst surface.

Mole balance of surface species

$$\sum_k\left(v_{k,j}R_k\right)=0 \tag{3}$$

where k is the index of reactions including adsorption, desorption and surface reactions; $v_{k,j}$ is the stoichiometric coefficient of component j in reaction k.

Conservation of active catalyst surface sites

$$\sum_j\left(\theta_j+\theta_v\right)-1=0 \tag{4}$$

where θ_j is the fractional coverage of surface species j, θ_v is the fraction of vacant sites.

Fluid energy balance

$$\rho_f c_{pf}\overline{u_f}\frac{\partial T_m}{\partial Z}+\frac{h_f}{R_\Omega}\left(T_m-T_s\right)=0 \tag{5}$$

where T_m, ρ_f and c_{pf} are temperature, density and heat capacity of the fluid, and h_f is the heat-transfer coefficient. The previous discussion on mass-transfer coefficients also applies to heat-transfer coefficient.

Adiabatic monolith energy balance

$$\delta_w k_w\frac{\partial^2 T_s}{\partial Z^2}-\overline{u_f}R_\Omega\left(\rho_f c_{pf}\frac{\partial T_m}{\partial Z}+C_T\sum_j\left(\frac{\partial X_{jm}}{\partial Z}H_j^0\right)\right)=0 \tag{6}$$

where δ_w is the half wall thickness (assuming symmetric structure of channels in a monolith reactor), k_w is the heat conductivity of the wall, H_j^0 is the standard formation enthalpy of gas component j. It should be mentioned that, in some previous studies,[21,22] energy balance of solid phase in the following form was used instead of Eq. 6

$$\delta_w k_w\frac{\partial^2 T_s}{\partial Z^2}-h_f\left(T_s-T_m\right)+\delta_c\sum_k\left[\left(-\Delta H_k\right)R_k\right]=0 \tag{7}$$

where $-\Delta H_k$ is the heat of surface reaction k. Since the monolith consists of solid and fluid phases, given other equations, the uses of Eqs. 6 and 7 are theoretically equivalent. However, the application of Eq. 7 involves ΔH evaluation for all surface reactions. Unfortunately, it is not uncommon that some of the reaction steps are considered irreversible in a microkinetic model (see the next section) and, as a result, the corresponding values cannot be easily obtained due to the lack of reverse activation energies. On the contrast, Eq. 6 is more convenient to implement in that it uses standard formation enthalpies of gas species, which are generally well tabulated in thermodynamics handbooks and databases. In addition, sequentially using Eqs. 6 and 5 can describe fluid and solid temperatures as functions of the fluid composition, reducing the number of unknowns involved in the steady-state calculations (see more details later in the section for model simplification). It should be noted that the simple form of energy balance equation was specifically derived for steady-state conditions ($\frac{\partial}{\partial t}=0$). Its applications to transient analyses cannot be generally justified due to the accumulation of surface species.

In the aforementioned model, Eqs. 2–4 are local functions, while Eqs. 1, 5 and 6 are differential equation. The boundary conditions are

$$X_{jm}\big|_{Z=0}=X_{jfeed} \tag{1a}$$

$$T_m|_{z=0}=T_{feed} \tag{5a}$$

$$\left.\frac{\partial T_s}{\partial Z}\right|_{Z=0}=\left.\frac{\partial T_s}{\partial Z}\right|_{Z=L}=0 \tag{6a}$$

where T_{feed} and $X_{j\text{feed}}$ are temperature and mole fraction of j in the feed.

Microkinetic model of NO/O_2/C_3H_6 system

As aforementioned, in order to realize continuous operation, reductants have to be introduced to the LNT during the reduction phase to reduce NOx and regenerate the NOx trapping catalysts for the use of the next cycle. Among the reductant candidates (CH, H_2, CO, NH_3, etc.), hydrocarbon is a nature choice because it is carried by the vehicles and ready to be accessed.[24, 25] In this study, hydrocarbon was represented by C_3H_6, consistent with the literatures.[7,8,21,22] In addition to NO, O_2 also presents in the feed to LNT even in the rich phase. Temperature effects on steady-state behaviors of NO/O_2/C_3H_6 system catalyzed by Pt/BaO/Al_2O_3 were investigated in this study using a detailed microkinetic model consisting of adsorption/desorption and surface reaction steps.

Compared with the previous microkinetic model,[7,21,22] three modifications were made in this work. First, the reaction steps involving barium were neglected. In this study, feed temperature is limited to 700 K for NO oxidation and 600 K for C_3H_6 oxidation. A parametric sensitivity analysis in our previous study showed that some reverse steps involved in NOx storage on BaO are very slow and the process is essentially irreversible at 613 K.[11] Yi et al. carried out temperature programmed desorption of NOx stored on BaO and found negligible $Ba(NO_3)_2$ decomposition up to 625 K.[26] Furthermore, they found that BaO_2 left on the surface during thermal decomposition of stored NOx at elevated temperatures is even more thermally stable than $Ba(NO_3)_2$.[26] Therefore, neglecting the reactions on barium is a reasonable

simplification in the steady-state calculations involved in this study. Second, the previous model assumes decomposive adsorption of O_2 directly forming O—Pt adatoms. In a more recent study, Divesh et al. found that molecular adsorption of O_2 on Pt surface is the rate limiting step of NO oxidation and should be accounted for.[9] The surface species, reaction steps, and rate constants were updated accordingly. Last, the previous model describes sequential C_3H_6 molecule adsorption and decomposition to CH_2—Pt surface species using two steps: $C_3H_6(g)+Pt \leftrightarrow C_3H_6-Pt$ and $C_3H_6-Pt+2Pt \rightarrow 3CH_2-Pt$. Since the latter decomposition step had been considered irreversible and there is no reaction between gas components and CH_2—Pt, the steady-state model has a temperature-independent solution with $\theta_{CH_2-Pt}=1$ and $R_k=0$ for all reactions. In order to avoid the trivial solutions, C_3H_6 adsorption and decomposition were lumped into a single reversible step. The finalized microkinetic model used in this study consists of the following steps

$$\text{S1} \quad NO(g)+Pt \leftrightarrow NO-Pt$$

$$\text{S2} \quad O_2(g)+Pt \leftrightarrow O_2-Pt$$

$$\text{S3} \quad NO-Pt+O-Pt \leftrightarrow NO_2-Pt+Pt$$

$$\text{S4} \quad NO_2(g)+Pt \leftrightarrow NO_2-Pt$$

$$\text{S5} \quad O_2-Pt+Pt \leftrightarrow 2O-Pt$$

$$\text{S6} \quad C_3H_6(g)+Pt \leftrightarrow 3CH_2-Pt$$

$$\text{S7} \quad CH_2-Pt+3O-Pt \rightarrow 4Pt+CO_2(g)+H_2O(g)$$

$$\text{S8} \quad CH_2-Pt+3NO-Pt \rightarrow 4Pt+CO_2(g)+H_2O(g)+1.5N_2(g)$$

$$\text{S9} \quad C_3H_6(g)+9O-Pt \rightarrow 9Pt+3CO_2(g)+3H_2O(g)$$

The temperature dependence of reaction rate constants was described by the Arrhenius expression

$$k_k=A_k\exp\left(\frac{-E_k}{RT_s}\right) \tag{8}$$

where k_k is the rate constant of reaction k, and A_k and E_k are the corresponding pre-exponential coefficient and activation energy, assumed independent of temperature and surface coverage. Rate expressions and kinetic parameters are summarized in Table 1.

In total, three overall reactions among NO, O_2 and C_3H_6 form CO_2, H_2O, NO_2 and N_2

$$\text{R1} \quad NO+0.5O_2 \leftrightarrow NO_2$$

$$\text{R2} \quad 9NO+C_3H_6 \rightarrow 4.5N_2+3H_2O+3CO_2$$

$$\text{R3} \quad C_3H_6+4.5O_2 \leftrightarrow 3CO_2+3H_2O$$

According to the microkinetic model, R1 and R2 can be described by the sequential addition of a number of microreaction steps

$$R1=S1+0.5S2+0.5S5+S3-S4 \tag{9}$$

$$R2=9S1+S6+3S8 \tag{10}$$

The overall C_3H_6 oxidation, however, can be realized via two pathways

$$R3_1=S6+4.5S2+4.5S5+3S7 \tag{11}$$

$$R3_2=4.5S2+4.5S5+S9 \tag{12}$$

It should be emphasized that the reactions involved in a realistic LNT can be more complicated than the description of aforementioned model, especially, due to the existence of hydrogen generated by the steam reforming of hydrocarbons and the water gas shifting of CO. Our previous studies[13,14] have shown that NO reduction by H_2 forms a complex product mixture containing N_2O, N_2, and NH_3 with the selectivity dependent on the feed composition and temperature. This modeling study was carried out based on previously reported experimental results.[9,21] These experiments were designed to probe the reaction mechanisms rather than to mimic realistic LNT conditions. For simplicity, H_2O and H_2 were not fed into the system. No significant formation of N_2O and NH_3 was observed during the experiments.[21] Therefore, we neglected these features accordingly in this study.

Table 1. Rate Expressions and Kinetic Parameters

step	Rate	A (mol/s/m^3)	E (kJ/mol)
$S1_f$	$kX_{NO,S}\theta_v$	7.5E9	0
$S1_r$	$k\theta_{NO-Pt}$	1.27E16	106.9
$S2_f$	$kX_{O2,S}\theta_v$	1.41E5	0
$S2_r$	$k\theta_{O2-Pt}$	1.74E13	80.0
$S3_f$	$k\theta_{NO-Pt}\theta_{O-Pt}$	4.5E14	101.3
$S3_r$	$k\theta_{NO2-Pt}\theta_v$	2.5E14	44.9
$S4_f$	$kX_{NO2,S}\theta_v$	8E9	0
$S4_r$	$k\theta_{NO2-Pt}$	5.7E17	97.9
$S5_f$	$k\theta_{O2-Pt}\theta_v$	4.94E18	80.0
$S5_r$	$k\theta^2_{O-Pt}$	1E22	209.4
$S6_f$	$kX_{C3H6,S}\theta_v$	3.33E5	7.3
$S6_r$	$k\theta^2_{CH2-Pt}$	1.68E19	179.7
$S7_f$	$k\theta_{CH2-Pt}\theta_{O-Pt}$	2.67E13	89.1
S8	$k\theta_{NO-Pt}\theta_{CH_2-Pt}$	2.58E22	188.5
S9	$k\theta_{O-Pt}X_{C3H6,S}$	3.43E5	11.2

Parameters from references[9,21]

Simplifications of the monolith reactor model

Three simplified versions of the steady-state monolith reactor model were developed and used in the calculations in this study. They are briefly introduced later.

Short Monolith (SM) Model. This model emphasizes the coupling of detailed surface reactions and transverse transport phenomena while neglecting all axial gradients. In our previous studies, SM model was used to simulate the steady-state behaviors of NO/H_2 [13] and NO/NH_3 [14] systems under isothermal conditions. It was extended in this study to include the reaction heat effects. Due to the assumption of complete back mixing, SM model consists of a set of material and energy balance equations that resemble those of a two-phase CSTR. Local Eqs. 2–4 remain valid while differential Eqs. 1, 5 and 6 become

$$\frac{\overline{u_f}}{L}\left(X_{jm}-X_{jfeed}\right)+\frac{k_{jc}}{R_\Omega}\left(X_{jm}-X_{js}\right)=0 \tag{13}$$

$$\rho_f c_{pf}\frac{\overline{u_f}}{L}\left(T_m-T_{feed}\right)+\frac{h_f}{R_\Omega}\left(T_m-T_s\right)=0 \tag{14}$$

$$\rho_f c_{pf}\left(T_m-T_f\right)+C_T\sum_j\left(X_{jm}-X_{feed}\right)H_j^0=0 \tag{15}$$

T_m and T_s can be straightforwardly calculated in sequence using Eqs. 15 and 14 as functions of product composition.

Piecewise Short Monolith (PSM) Model. Heat conduction in the solid phase is neglected, i.e., $k_w=0$. The axial concentration and temperature gradients, on the other hand, are accounted for by dividing the monolith reactor into a

number of short pieces. The interaction between two adjacent pieces is limited to the unidirection convection of gas flow. PSM is, therefore, a tank-in-series model. The discretized form of Eqs. 1, 5 and 6 are

$$\frac{\overline{u_f}}{\Delta Z}\left(X_{jm}^{M}-X_{jm}^{M-1}\right)+\frac{k_{jc}}{R_\Omega}\left(X_{jm}^{M}-X_{js}^{M}\right)=0 \tag{16}$$

$$\frac{\rho_f c_{pf}\overline{u_f}}{\Delta Z}\left(T_m^{M}-T_m^{M-1}\right)+\frac{h_f}{R_\Omega}\left(T_m^{M}-T_s^{M}\right)=0 \tag{17}$$

$$\rho_f c_{pf}\left(T_m^{M}-T_m^{M-1}\right)+C_T\sum_j\left(X_{jm}^{M}-X_{jm}^{M-1}\right)H_j^0=0 \tag{18}$$

where $\Delta Z=\frac{L}{NM}$ is the equally spaced step size along axial direction, NM is the number of mesh points ($1\le M\le NM$), and when $M=1$, $M=1$, $M-1=0$ corresponds to the feed defined by the boundary conditions. T_m and T_s of different monolith pieces can be individually solved using Eqs. 17 and 18, similar to the case of the SM model.

Uniform Wall Temperature (UWT) Model. On the contrast to the PSM model, infinitely fast heat conduction in the monolith wall is assumed, i.e., $k_w=\infty$. As a result, the wall temperature is uniform along the axial direction. The discretized Eqs. 16 and 17 are still valid for $1\le M\le NM$. However, due to the uniform wall temperature assumption, the monolith energy balance applies only once for the whole reactor

$$\rho_f c_{pf}\left(T_m^{NM}-T_{feed}\right)+C_T\sum_j\left(X_{jm}^{NM}-X_{jfeed}\right)H_j^0=0 \tag{19}$$

Equation 19 can be used to calculate the outlet gas temperature T_m^{NM}, which is then substituted to Eq. 17 to solve the uniform solid temperature by

$$T_s=\alpha_{NM}/\beta_{NM} \tag{20}$$

where $\beta_1=-1$, $\beta_i=-1+\beta_{i-1}\frac{\lambda}{\lambda+1}$ for $2\le i\le NM$; $\alpha_1=\lambda T_{\text{feed}}$, $\alpha_i=\alpha_{i-1}\frac{\lambda}{\lambda+1}$, for $2\le i\le(NM-1)$, $\alpha_{NM}=\alpha_{NM-1}\frac{\lambda}{\lambda+1}-(\lambda+1)T_m^{NM}$; $\lambda=\frac{\rho_f c_{pf}\overline{u_f}R_\Omega}{h_f\Delta Z}$. T_s is required to evaluate reaction rate constants. However, according to the previously described monolith model, it is not necessary to further calculate fluid temperature that has no effect on the material balance equations. In the case that internal fluid temperature profile is of interests, T_m values at different axial mesh points can be evaluated by

$$T_m^{M}=\left(T_s+\lambda T_m^{M-1}\right)/(\lambda+1)\ \text{ for}\ 1\le M\le(NM-1) \tag{21}$$

As such, in the use of all three simplified models, temperatures can be described as functions of fluid composition and do not count for unknowns during the calculation of steady-state solutions. Furthermore, noticing that the rates of all gas involved reaction steps are linear with respect to gas concentrations, washcoat concentrations (X_{js}) of all gas species can be analytically eliminated by applying Eq. 2. Theoretically, using Eq. 4 can further eliminate one of the surface species as a model unknown. However, it was found that the fractional surface coverage's of some surface species may vary by tens of magnitude orders at different temperatures. Equation 4 was, therefore, retained in the calculations to avoid the inaccuracy that may be introduced by truncation errors. Finally, since the formations of CO_2, N_2 and H_2O were considered irreversible (S7, S8, and S9) and have no effect on other components, at steady state; their concentrations can be directly calculated from the conservation of N, C and H atoms. In all, the discretized monolith reactor model, after consolidating with the microkinetics, is in the form of a nonlinear equation system that has a total unknown number of

$$N=NM(4+6) \tag{22}$$

where the number 4 is for gaseous species, NO, C_3H_6, O_2 and NO_2; 6 is for surface species NO—Pt, CH_2—Pt, O_2-Pt, O—Pt, NO_2-Pt and v-Pt. Noted is that both PSM and UWT models reduce to the SM model as $NW=1$.

In this study, feed temperature T_{feed}, was used as the independent bifurcation variable, in consistence with experiments. The problem of parameter dependent solutions to a nonlinear system was solved using a simplified pseudo-arclength continuation method that is separately described in the Appendix. All calculations were performed on a DELL VOSTRO personal computer equipped with a 2.1GHz Intel Core 2 Duo processor.

Results and Discussion

In this section, the model predictions are presented and compared with experimental measurements reported in literatures.[9,21] All experimental data had been acquired on a bench scale setup essentially consisting of a feed system, a tube reactor and a data acquisition system. Various feed compositions were obtained by several mass flow controllers connected to different gas cylinders. The mixed gas was heated with a tube furnace before being fed to the reactor. The monolith catalyst containing Pt and BaO loaded on γ-alumina wash coat was provided by BASF Catalysts LLC and then cut to the desired shape in the laboratory. The inlet gas and catalyst temperatures were measured using thermocouples. Effluent composition was analyzed using FTIR spectrometer, oxygen analyzer, and total hydrocarbon analyzer. More detailed descriptions can be found elsewhere.[3–6,9,21]

NO oxidation

Pt catalyzed NO oxidation was systematically investigated by Divesh et al., who found that adsorption of O_2 molecules on Pt surface is the rate limiting step and then developed an overall rate expression using the microkinetic model consisting of five reversible steps (S1–S5). It was also found that the catalytic activity of alumina supported Pt is reduced after the addition of barium. In order to account for this activity reduction, we assumed that the volumetric reaction rates are proportional to active Pt concentration and all rate constants are reduced by the same deactivation factor for the Pt/Ba/Al catalyst[11] i.e.

$$A_k=A_k^0/f_{deac} \tag{23}$$

where A_k^0 is the originally reported pre-exponential, k is for each reaction involved in steps S1–S5. The calculations were carried out using physical properties and monolith reactor parameters summarized in Table 2.

In this study, conversion of component j was defined as

$$\text{Conv}_j=\frac{\left(X_{j,\text{feed}}-X_{j,m}^{NM}\right)}{X_{j,\text{feed}}} \tag{24}$$

Figure 1 shows the comparison between experimentally measured NO conversion on the Pt/Ba/Al catalyst and calculation results by the PSM model with various NM numbers

Table 2. Model Parameters in the Calculation of NO Oxidation

$D_{m,O2}$	4.57E-5(m^2/s)	$D_{m,NO}$	4.57E-5(m^2/s)
$D_{m,NO2}$	3.42E-5(m^2/s)	H^0_{NO2}	33.1(kJ/mol)
H^0_{NO}	90.29(kJ/mol)	L	0.0154(m)
u_f	0.316(m/s)	R_Ω	2.75E-4(m)
C_T	38.1(mol/m^3)	δ_c	1.45E-5(m)
$X_{O2,feed}$	0.05	$X_{NO,feed}$	5.28E-4

Parameters in consistence with experimental conditions

and $f_{\text{deac}} = 5$. It has been shown by Balakotaiah et al. [27] that an SM model is quantitatively accurate when the transverse Peclet number defined below is greater than unity

$$P = \frac{\overline{u_f} R_\Omega^2}{L D_m} \approx \frac{\overline{u_f} R_\Omega}{L k_c} \tag{25}$$

Using the parameters provided in Table 2 gives $P \approx 0.034$ for NO. The required mesh point number can, therefore, be estimated to be 30. It may be seen from the figure that model predicted NO conversion increases with increased *NM* in the middle temperature range of about 400–700 K, which is due to the enhanced mass transfer with more mesh points. This effect is diminished when *NM* is greater than 30, and the model predictions are in good agreements with experimental data. At temperatures lower than 400 K, the conversion is controlled by kinetics to a very low level. On the other side, at temperatures higher than 700 K, conversion of exothermic NO oxidation is controlled by thermodynamics and the predicted curves with various *NM* values converge to the equilibrium limits. Applying Eq. 16 and assuming negligible NO concentration in the solid phase can give an estimate to the mass-transfer limited conversion

$$conv_{mt} = 1 - \left(\frac{P_\Delta}{P_\Delta + 1}\right)^{NM} \tag{26}$$

where $P_\Delta = \frac{\overline{u_f} R_\Omega}{\Delta Z k_c} = P \times NM$. The calculated conv_{mt} for $NM = 30$ is essentially complete, whereas the maximum NO conversion is limited to 0.8 around 600 K as shown in Figure 1. This indicates that, in addition to mass transfer, kinetics and thermodynamics also have significant effects on the overall conversion.

In order to efficiently solve the steady-state model, it is desired to reduce the number of unknowns, which is proportional to *NM* according to Eq. 22. Figure 1 shows that, with decreased *NM*, the predicted maximum NO conversion decreases and slightly shifts toward higher temperatures. An *NM* value of 5 gives quantitatively reasonable predictions and the SM model ($NM = 1$) is capable of catching the qualitative trends.

It should also be mentioned that, due to the low NO concentration in the feed and the relatively low-reaction heat of R1, the temperature variation during NO oxidation is less than 1 K.[9] The process is, therefore, essentially isothermal. In this case, PSM and UWT models are equivalent and reduce to the lumped thermal (LT) model that has been presented elsewhere.[14]

The distribution of surface species calculated using SM model is plotted in Figure 2 as a function of temperature. It

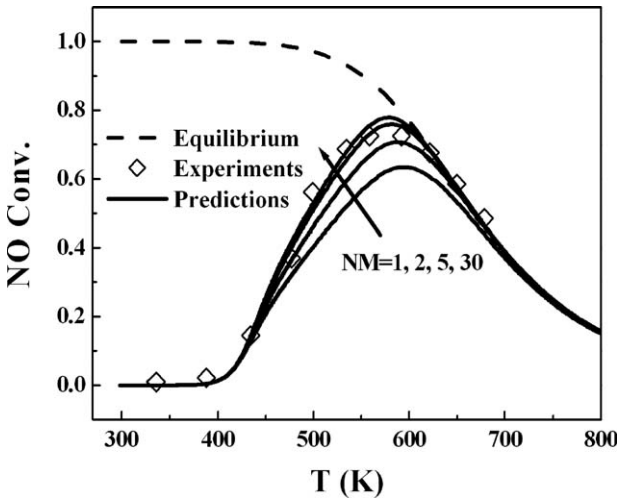

Figure 1. Comparison between experimentally measured conversion of NO oxidation and model predictions.

is seen that Pt surface is mainly covered by NO—Pt admolecules in the low-temperature range. At about 400 K, NO—Pt is replaced by O—Pt and the conversion of overall reaction R1 becomes observable. O—Pt is dominant on the surface up to about 700 K. At higher temperatures, oxygen desorption (the reverse of step S5) with an activation energy of 209 kJ/mol is activated. As a result, O—Pt adatoms are replaced by vacant sites and the conversion becomes thermodynamically controlled. The fractional coverages of O_2-Pt and NO_2-Pt are maintained at low levels of about 10^{-4} in the entire temperature range.

In the case of NO oxidation, the simulations predicted that NO conversion is a single valued function of the feed temperature, which is in agreement with the results reported by Divesh et al., who measured each data point after as long as few hours to achieve the pseudo-steady state.[9] It should be noted that Hauptmann et al. observed hysteresis of Pt catalyzed NO oxidation during temperature programmed light-off/light-down-experiments with both heating and cooling rates being 0.083 K/s (5°C/min).[28] The interesting

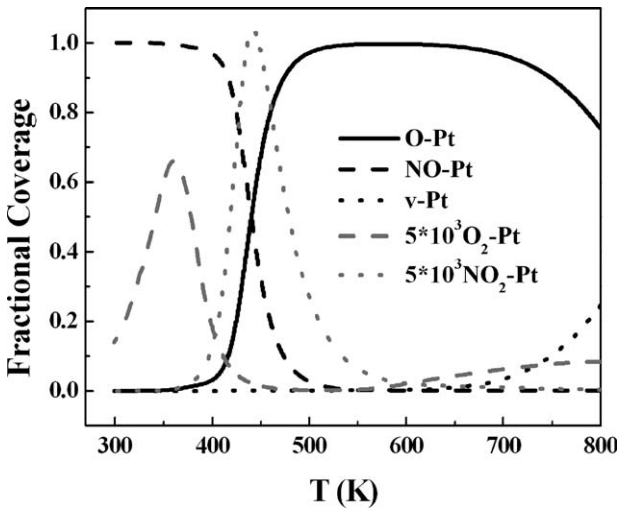

Figure 2. Calculated fractional coverages of surface species involved in NO oxidation (SM model).

Table 3. Model Parameters in the Calculation of C_3H_6 Oxidation

k_{c,C_3H_6}	0.08(m/s)	$k_{O_2,c}$	0.134(m/s)
$k_{NO,c}$	0.1544(m/s)	$k_{NO_2,c}$	0.124(m/s)
H^0_{CO2}	−393.5(kJ/mol)	H^0_{H2O}	−240.8(kJ/mol)
H^0_{C3H6}	20.41(kJ/mol)	C_T	30.46(mol/m^3)
$\rho_f c_{Pf}$	600(J/m^3/K)		
h_f	100(w/m^2/K)	c_{pw}	1000(J/kg/K)
L	0.02(m)	u_f	5(m/s)
R_Ω	5E-4(m)	δ_c	2.0E-5(m)

Parameters in consistence with experimental conditions[21]

phenomenon that extinction temperature is higher than ignition temperature during this transient process was referred to as "reverse hysteresis"[28] They explained this feature by introducing an intermediate of "Pt_Ox", which is formed by reversible NO_2-Pt decomposition releasing gas NO, different from Pt-O formed via oxygen adsorption. Pt_Ox, and the corresponding reaction step were not taken into account in the current steady-state study mainly for two reasons. First, it was pointed out in the same work that, at steady state, the catalyst activity is independent of temperature history and the hysteresis should disappear.[28] Second, when hydrocarbon, a stronger reductant than NO, is added to the system, it should be able to react with Pt_Ox and regenerate the catalyst. However, to the best of our knowledge, relative kinetic studies have not been reported in the literature. In the current stage of our study, the NO oxidation model consisting of S1–S5 is adequate to quantitatively explain the experimental data (see Figure 1). More importantly, as will be shown in the following sections, the use of S1–S5, and the corresponding parameters can be directly extended to the cases with C_3H_6 added to the feed mixture.

C_3H_6 oxidation

Physical properties and monolith reactor parameters used in the following calculations are summarized in Table 3. During the calculations, the feed concentrations of O_2 to C_3H_6 were set at 2% and 0.2%, unless otherwise mentioned. Oxygen is in excess according to overall reaction R3. The adiabatic temperature rising for complete hydrocarbon conversion can be estimated by

$$\Delta T_{ad} = \frac{(-\Delta H_{R3}) C_T X_{CH,\text{feed}}}{\rho_f c_{pf}} \tag{27}$$

Using Eq. 27 and parameters in Table 2 gives 195 K. Different from the previously discussed isothermal NO oxidation process, the combustion of 0.2% C_3H_6 is highly exothermic and the fluid temperatures may be considerably higher than that of the feed under adiabatic condition.

Calculated hydrocarbon conversions using PSM, UWT and SM models are compared in Figure 3. It may be seen that C_3H_6 oxidation exhibits typical multiple steady states of an exothermic system. The UWT model predicts an "S" shape that can be divided into low conversion, transition and high-conversion regimes. The low-conversion regime is controlled by slow kinetics at low temperatures. In the transition regime, conversion increases with decreased feed temperature. These solutions are unstable and cannot be obtained by integrating the transient model. In the high-conversion regime, conversion increases with increased temperature, indicating important kinetic effects. In addition, UWT model predicts enhanced mass transfer in the whole monolith reactor with increased *NM*. As a result, the predicted conversions increase and the extinction point are shifted toward lower temperatures. The model predictions by *NM* values equal to 5 and 3 are very close, suggesting again that be sufficient to give quantitatively reasonable results. Calculations with more mesh points were, therefore, not carried out.

The PSM model predicts more than three solution branches and the branch number increases with increased *NM* ($N_{\text{solution}} = 2NM + 1$). According to the calculations results, if the M^{th} piece of short monolith is ignited, those numbered higher than *M* must be ignited. In the PSM model, the adjacent short monoliths are connected only by unidirectional convection of the fluid. In addition, the quenched pieces are essentially inert due to the low conversion in this regime. Therefore, each piece sequentially ignited from the outlet or quenched from the inlet is fed with a fluid that has the same composition and temperature as those in the feed. As a result, the ignitions of all pieces occur at the same feed temperature. Similar are the extinction points at a fixed *NM*. However, when *NM* is decreased, the extinction point is shifted toward lower temperatures, which is opposite to the trend of UWT model. In the case of the PSM model, the extinction occurs piecewisely rather than for the whole monolith reactor. Decreased *NM* corresponds to an increased length of each individual monolith piece. PSM model featured by piecewise ignition and extinction predicts enhanced mass transfer in this increased length, which is responsible for the extension of high-conversion regime to lower temperatures. It has been shown that, in the absence of axial dispersion, the monolith model is in the form of a differential algebraic equation (DAE) system and may have infinite number of solutions if local multiplicity exists.[13] The discretized form of the PSM model uses the first-order backward approximation of $\partial/\partial Z$ terms appearing in Eqs. 1 and 5. This treatment introduces numerical dispersions and as $NM \gg 1$, $\text{Pe} = \text{Pe}_H = 2NM$, where $\text{Pe} = \frac{L\overline{u_f}}{D_{ax}}$, $\text{Pe}_H = \frac{L\overline{u_f}\rho_f c_{pf}}{\kappa_f}$, D_{ax} and κ_f are axial diffusivity and heat conductivity of the fluid. Due

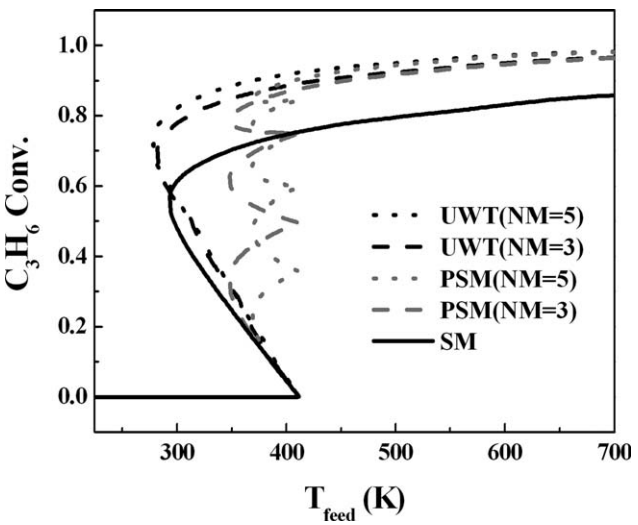

Figure 3. C_3H_6 conversion calculated using different models and varied number of mesh points.

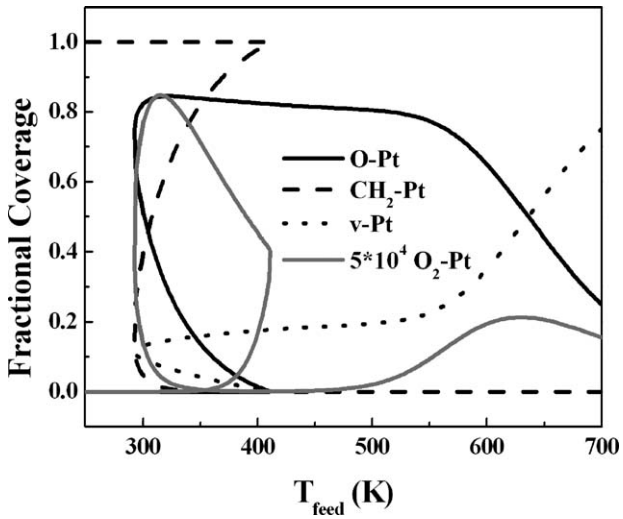

Figure 4. Calculated fractional coverages of surface species involved in C_3H_6 oxidation (SM model).

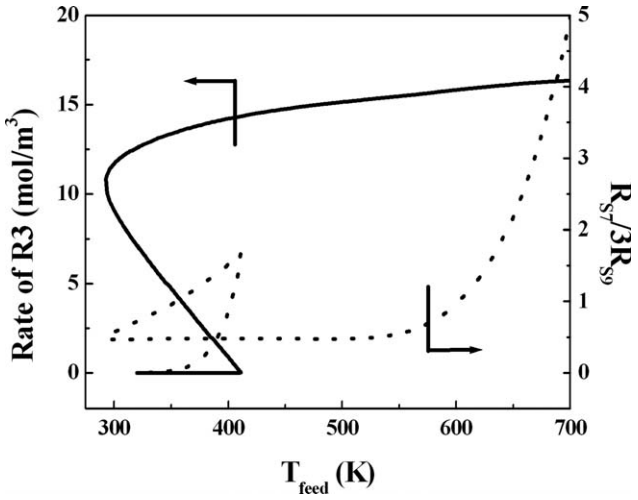

Figure 5. Total C_3H_6 oxidation rate and the ratio of two reaction pathways (SM model).

to these numerical axial dispersions, the number of solution branches is reduced to a finite value.

Figure 3 shows that as $NM = 1$, both the UWT and PSM models reduce to the SM model, from the left and right sides, respectively. The SM model predicts three branches similar to the UWT model, but with lower conversions in the ignited regime due to the assumption of complete back mixing. Noted is that all three models predict the same ignition point located at 411 K, which is mainly determined by kinetics. The aforementioned comparison shows that the SM model is capable of catching the major trends of the discretized models, especially, the ignition point. Since the SM model has a reduced unknown number and is easy to solve, it will be used in the following discussion.

The calculated fractional coverages of various surface species are plotted in Figure 4 as functions of feed temperature. It may be seen that the coverage of O_2-Pt is limited to the magnitude order of 10^{-6} for the whole temperature range. CH_2—Pt is the major surface species before ignition. In the transition regime, CH_2—Pt is desorbed and replaced by O—Pt and vacant sites. Different from the previous case of NO oxidation, O—Pt coverage is limited to about 0.85, which can be attributed to its reaction with gas C_3H_6 via step S9. In the high-conversion regime, O—Pt coverage gradually decreases with increased temperature to the level of 0.8 at about 600 K, where the decrease becomes accelerated due to the activation of oxygen desorption. According to the microkinetic model, C_3H_6 oxidation can be realized via two pathways described as Eqs. 11 and 12. Figure 5 shows that the overall rate of R3 ($= R_{S7}/3 + R_{S9}$) has the same trend as that of C_3H_6 conversion and exhibits an S shape when plotted against feed temperature. C_3H_6 consumption rates of the two pathways are comparable in the entire temperature range. In the low-conversion regime, due to the relatively higher activation energy, R_{S7} increases more rapidly than R_{S9} with increased temperature. Step S7, is, therefore, a controlling step for the ignition.

C_3H_6 oxidation is a typical exothermic system that exhibits multiple steady-states due to the coupling of nonlinearly temperature-dependent heat generation and linear heat removal.[29] Our previous studies also showed that multiplicity may exist even under isothermal conditions due to the nonlinearity of kinetics.[13,14] In this work, we carried out numerical experiments for the same C_3H_6/O_2 feed under isothermal conditions by forcing $T_s = T_{feed}$. On the contrary to the adiabatic assumption, this physically corresponds to a cooling system set at the feed temperature and operated with infinite heat removing efficiency. Calculated C_3H_6 conversion exhibits multiplicity in a temperature range of 396–411 K as shown in Figure 6. In this range, similar to the trends shown in Figure 4, the surface can be occupied by either CH_2—Pt or O—Pt, corresponding to quenched and ignited branches, respectively (the surface species distribution plot is omitted here for conciseness). This phenomenon of catalyst surface competition induced multiplicity was referred to as "surface explosion".[30] Compared with the adiabatic value, the ignition temperature is barely changed, indicating negligible reaction heat effects at low conversions. On the other hand, the extinction temperature is increased by about 103 K, and the conversion in the ignited regime is notably reduced. Since mass-transfer coefficients were assumed constant, these features again suggest significant kinetic effects in the high-

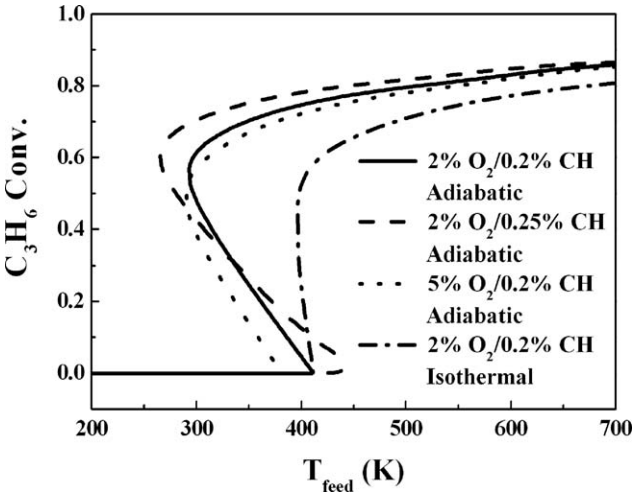

Figure 6. Comparison of model predictions under adiabatic and isothermal conditions and effects of feed composition (C_3H_6 oxidation, SM model).

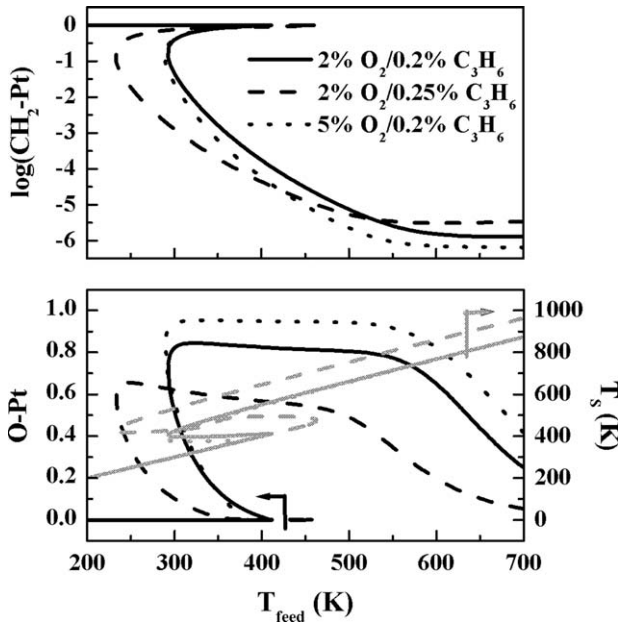

Figure 7. Calculated fractional coverages of CH_2—Pt and O—Pt and solid temperature for various feed compositions (SM model).

conversion regime. Furthermore, the UWT model assuming uniform wall temperature predicts three solution branches independent of *NM*, while the PSM model predicts more solution branches with increased *NM* (see Figure 3), indicating that reaction heat induced multiplicity is dominant under adiabatic conditions.

Figure 6 also shows effects of reactant concentrations in the feed on steady-state C_3H_6 oxidation. As aforementioned in the previous discussion (see Figure 4), the system is ignited when CH_2—Pt is desorbed and the surface is occupied by O—Pt adatoms. As C_3H_6 concentration is increased from 0.2 to 0.25%, a higher temperature is required for O—Pt to dominate in the surface competition, and, as a result, the ignition temperature is increased from 411 K to 449 K. For the same reason, as O_2 concentration is increased from 2 to 5%, the ignition temperature is decreased to about 382 K. Noted is that the trend of delayed ignition with decreased O_2 concentration is in agreement with experimental observations.[21] In the ignited regime, increasing C_3H_6 concentration results in higher conversions and the extinction point shifted to a lower temperature at about 265 K, which cannot be simply explained by the surface distribution. Figure 7 shows that, compared with the case of 0.2% C_3H_6 (solid), O—Pt coverage (dash) is reduced while CH_2—Pt can be either higher or lower under different temperatures. Considering that the conversion is partially determined by kinetics in the ignited regime, this enhanced conversion can be attributed to the extra reaction heat generated by the combustion of additional C_3H_6 (see solid temperature presented in the gray curves). While the increase in feed O_2 concentration (dot) does not have significant effects on solid temperature, it does affect the surface species distribution. Figure 7 illustrates contradicting effects of increased O_2 concentration on the two pathways of C_3H_6 oxidation defined in Eqs. 11 and 12. First consider step S7 between O—Pt and CH_2—Pt. With increased O_2 in the gas phase, O—Pt coverage increases from about 80% to the level of about 95%. CH_2—Pt coverage, however, is consistently lower than that of the reference case with 2% O_2 in the feed. This decrease in CH_2—Pt is more profound than the increase in O—Pt. As a result, the rate of S7 is reduced. On the other hand, increased O—Pt coverage corresponds to a higher rate of step S9, the other C_3H_6 oxidation pathway. The overall result of these two compensating effects is a slightly reduced conversion in the ignited regime. The kinetic effects are diminished at further elevated temperatures, and, as a result, conversions of all three feeds approach the same limit determined by mass transfer.

C_3H_6 oxidation with the presence of NO

The previously discussed system was added with NO. The addition of NO plays two roles in this system. It can either be oxidized to NO_2 by O_2 via overall reaction R1 or be reduced to N_2 by C_3H_6 via overall reaction R2. The feed mixture contains 5% O_2, 0.2% C_3H_6 and 500 ppm NO, consistent with the experimental conditions.[21] The experimental results are presented in Figure 8, where NOx refers to NO + NO_2 and conversion is defined in Eq. 24.

Using the model parameters listed in Table 2, C_3H_6 conversion, NOx conversion, solid temperature, and fractional coverages of surface species at steady states were calculated as functions of temperature. The results are shown in Figure 9a and 9b. At temperatures lower than 380 K, the surface is mainly covered by CH_2—Pt and conversions of both CH and NOx are negligible. With increased temperature, CH_2—Pt is first replaced by NO—Pt admolecules. While an O_2-Pt peak of about 10^{-4} is also formed, O—Pt is maintained at a very low level. The main overall reaction in this regime is R3 and NO is partially reduced to N_2 by C_3H_6. Both NOx and C_3H_6 conversions increase slightly with increased temperature up to 452 K. At 452 K, the system is ignited and the surface becomes dominated by O—Pt. Due to the

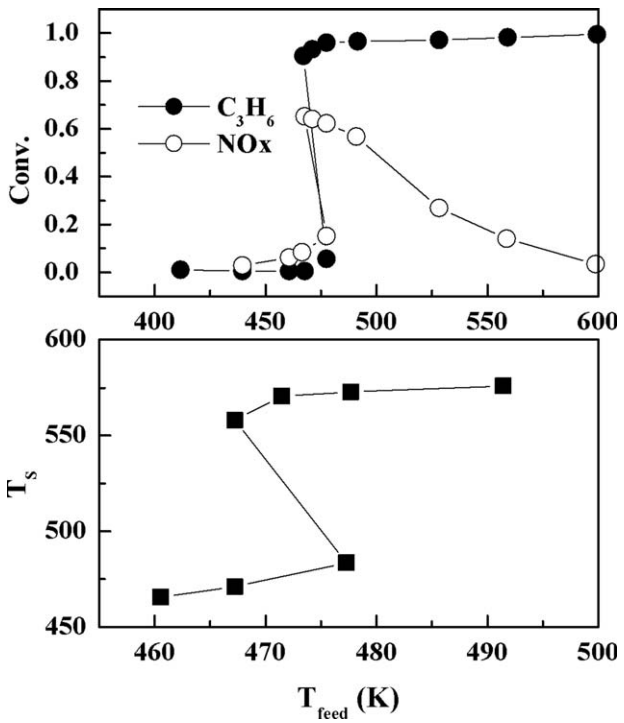

Figure 8. Experimentally measured C_3H_6, NO conversion and solid temperatre for a feed mixture containing 5% O_2, 0.2% C_3H_6 and 500 ppm NO.

competition between NO oxidation and NO reduction, NOx conversion first decreases and then increases with increased temperature.

The model predictions capture some of the important experimentally observed features such as multiplicity, delayed ignition point with the addition of NO (from 382 K to 452 K; compare dot curve in Figure 6 and solid curve in Figure 9a), and the noteworthy observation of NOx conversion hysteresis with a maximum at a temperature lower than the ignition point. However, several apparent inconsistencies do exist between model predictions and experimental data as summarized in Table 4.

In order to improve the model predictions, two of the kinetic parameters were modified based on a systematic parametric sensitivity study[11,14] that is not reported here for brevity. E_{f7} and A_{f8} were reset to be 110 kJ/mol and 2.6E20 mol/m^3/s, respectively. Furthermore, Eq. 15 for T_m calculation is modified with an additional factor

$$\rho_f c_{pf}\left(T_m - T_f\right) + 0.6 C_T \sum_j \left(X_{jm} - X_{\text{feed}}\right) H_j^0 = 0 \qquad (15a)$$

The calculated conversions and solid temperature are plotted against feed temperature in Figure 9c. It may be seen from Table 4 that model predictions with modified parameters are in better agreement with the experimentally measured data. Eq. 15a assumes that only 60% of the reaction heat contributes to the fluid temperature rising. It is acknowledged that this is a simple treatment accounting for heat loss to the environment. A more detailed model description requires evaluation of the transverse temperature gradient among different monolith channels, which is beyond the scope of this study.

This work is focused on the steady-state behaviors of NO/C_3H_6/O_2 system. It has been reported multiplicity may exist also for the cyclically operated NSR process.[21] Bifurcation analysis of a NOx after-treatment process carried out in a multicolumn system was studied by Fissore et al. for the case of fast switch operations.[31] The multiplicity of cyclic NSR process will be investigated in a future study.

Table 4. Comparison of Model Predictions with Experimental Results

Feature	Experiments	Predictions[a]	Predictions[b]
Ignition point	477 K	452 K	473 K
Extinction point	465 K	400 K	448 K
$(T_s\text{-}T_{feed})$	100 K	177 K	101 K
NOx conversion	Monotonically decreases	Fist decrease and then increase	Monotonically decreases

[a]Calculated using kinetic parameters in Table 1; shown in Figure 9a and 9b
[b]Calculated using modified parameters; shown in Figure 9c

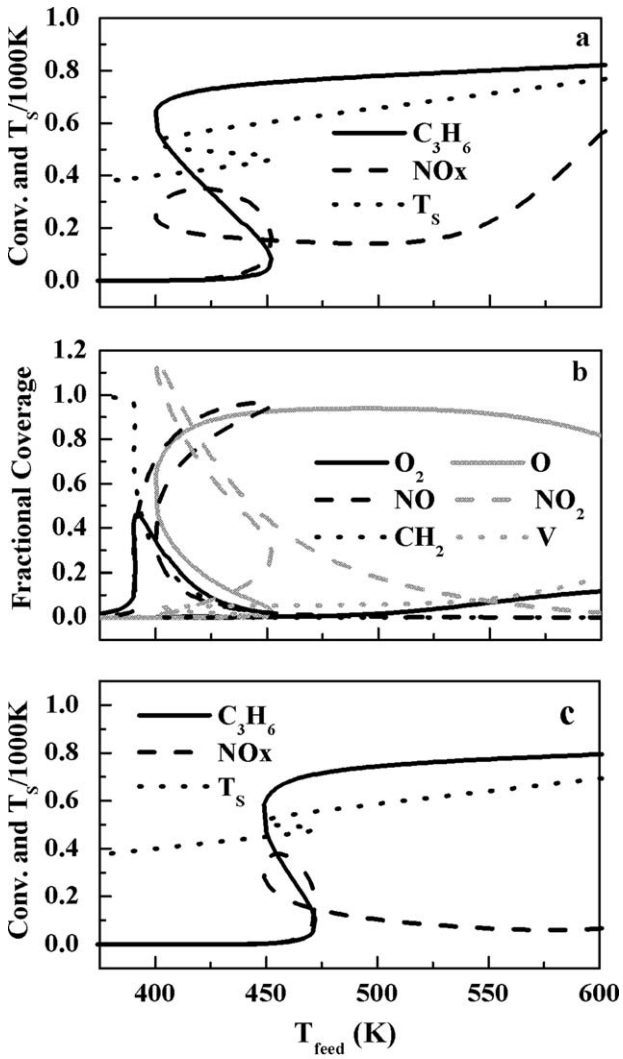

-1-

Figure 9. SM model predictions for a feed mixture containing 5% O_2, 0.2% C_3H_6 and 500 ppm NO.

(a) Conversions and solid temperature calculated using the original parameters, (b) fractional coverages of surface species (values of O_2-Pt and NO_2-Pt are multiplied by 1^*10^4 and 5^*10^4, respectively), and (c) conversions and solid temperature calculated using modified parameters.

Conclusions

In this study, temperature effects on steady-state behaviors of several feeds with various NO/O_2/C_3H_6 ratios were theoretically investigated. A steady-state monolith reactor model was proposed accounting for reaction heat effects. An overall enthalpy balance equation using standard formation enthalpies of gas species was introduced. This treatment does not involve the reaction heat of each individual surface reaction that is difficult to evaluate but required by conventionally used solid energy balance equation. Three simplified versions of the monolith model, namely, SM, PSM and UWT models, were developed based on various assumptions on the axial gradients. The literature reported microkinetic model was updated according to the latest research findings and to avoid trivial solutions. The steady-state model was rigorously solved using a pseudo-arclength method that is capable of going over the bifurcation points and simple to implement due to the avoidance of explicit Jacobian matrix evaluation. A total of three cases were investigated.

Oxidation of 500 ppm NO is essentially isothermal and, as a result, PSM and UWT models are equivalent. The catalytic activity of alumina supported Pt is reduced after the addition of barium. Using a constant deactivation factor for all involved reaction steps can efficiently account for this activity reduction, which is validated by the quantitatively good agreement between model predictions and experimental

measurements. At low temperature, Pt surface is dominated by NO—Pt and the rate of NO oxidation is slow. NO—Pt is gradually replaced by O—Pt with increased temperature up to 700 K, where oxygen desorption occurs and the system becomes thermodynamically controlled. In the investigated temperature range, NO conversion is determined by the combined effects of mass transfer, kinetics and thermodynamic equilibrium. Both experiments and simulations showed that multiplicity does not exist.

In the case of C_3H_6 oxidation, however, significant reaction heat effects the result in typical multiple steady states for an exothermic system. CH conversion vs. feed temperature predicted by UWT model and SM model is in the form of an S shape that can be divided into low conversion, transition and high-conversion regimes. PSM model predicts more solution branches with increased *NM* because the monolith reactor can be piecewisely ignited from the outlet and quenched from the inlet. The ignition point is kinetically controlled and identical for both models with varied NM values. The high-conversion regime and the extinction point, on the other hand, are more complicated and dependent on the model and NM value as well, which can be explained by the combined effects of kinetics and mass transfer. According to the microkinetic model, C_3H_6 oxidation can be realized via two pathways. Calculation results showed that the rates of these two pathways are comparable in the entire temperature range. In addition to reaction heat effects, the kinetic nonlinearity, by itself, leads to multiple steady states even under isothermal conditions. A comparison showed that the reaction heat induced multiplicity is dominant under adiabatic conditions. Ignition of C_3H_6 oxidation is featured by the replacement of CH_2—Pt with O—Pt, and, as a result, higher temperatures are required for ignition with increased C_3H_6 or decreased O_2 in the feed, which is in agreement with experimental results. Qualitative and quantitative analyses of surface species and surface reaction rates were used to explain composition effects on the conversion and extinction point.

A comparison showed that the SM model is capable of catching the major trends of the discretized models. It was, therefore, used to investigate the final case of C_3H_6 oxidation with the presence of NO. Added NO can react with both C_3H_6 and oxygen, forming N_2 and NO_2, respectively. Calculation results were compared with experimental measurements in terms of CH conversion, NOx conversion and monolith temperature. The model captures some of the major experimental trends, such as multiplicity, delayed ignition point with the addition of NO, and the noteworthy observation of NOx conversion hysteresis with a maximum at a temperature lower than the ignition point. Some quantitative discrepancies including ignition point, extinction point, monolith temperature, and the trend of increased NOx conversion at high temperatures that had not been experimentally observed in the temperature range of interests, were corrected by tuning few of the model parameters.

In addition to discuss the multiplicity of the $NO/C_3H_6/O_2$ system, we proposed a monolith reactor model with revised energy balance equations, derived and compared three model versions under different conditions, and presented a simplified pseudo-arclength method. These simplifications in the steady-state modeling of catalytic monolith reactors should be capable of providing theoretical assistance to relative studies in the future.

Acknowledgment

This work is supported by Zhejiang Provincial Natural Science Foundation (Y5100296), Qianjiang Program of Zhejiang Science and Technology Dept. (2012R10070) and China Natural Science Foundation (21376181). The graduate courses of Wei Xu and Meng-Long Lai are financially supported by Zhejiang Provincial Natural Science Foundation (Y5110174) and China Natural Science Foundation (21106108), respectively. The authors thank Dr. Clayton at Caterpillar, Inc. for the valuable discussions that have directly inspired this study.

Notation

A = pre-exponential kinetic constant, mol s^{-1} m^{-3}
c_p = heat capacity, J kg^{-1} K^{-1}
C_T = gas-phase concentration, mol m^{-3}
D_m = molecular diffusivity, m^2 s^{-1}
E = activation energy, kJ mol^{-1}
h_f = heat-transfer coefficient, w m^{-2} K^{-1}
H^0 = standard formation enthalpy
k = kinetic constant, mol s^{-1} m^{-3}
k_c = mass-transfer coefficient, m s^{-1}
L = monolith length, m
N = unknown number
R = universal gas constant, 8.314 J mol^{-1} K^{-1}; reaction rate, mol m^{-3} s^{-1}
R_Ω = effective transverse length scale, m
s = pseudo arc-length
T = temperature, K
u_f = mean fluid velocity, m s^{-1}
x,y = unknown variable
X = mole fraction

Greek letters

δ_c = washcoat thickness, m
ΔH = reaction heat, J mol^{-1}
θ = fractional coverage of surface species
ρ = density, kg m^{-3}
v = stoichiometric coefficient

Subscripts

ad = adsorption
de = desorption
f = feed, forward reaction
G = gas
i = index of gaseous components
j = index of surface species
k = index of microreaction steps
m = bulk phase
r = reverse reaction
s = solid phase

Literature Cited

1. Takahashi N, Shinjoh H, Iijima T, Suzuki T, Yamazaki K, Yokota K, Suzuki H, Miyoshi N, Matsumoto S, Tanizawa T, Tanaka T, Tateishi S, Kasahara K. The new concept 3-way catalyst for automotive lean-burn engine: NOx storage and reduction catalyst. *Catal Today*. 1996;27:63–69.
2. Harold MP. NOx storage and reduction in lean burn vehicle emission control: a catalytic engineer's playground. *Curr Opin Chem Eng*. 2012;1:1–9.
3. Kabin KS, Muncrief RL, Medhekar V, Harold MP. NOx storage and reduction on a Pt/BaO/alumina monolith storage catalyst. *Catal Today*. 2004;96:79–89.
4. Muncrief R. Khanna P, Kabin K, Harold MP. Mechanistic and kinetic studies of NOx storage and reduction on Pt/BaO/Al_2O3. *Catal Today*. 2004;98:393–402.
5. Muncrief R, Kabin K, Harold MP. NOx storage and reduction with propylene on Pt/BaO/Alumina. *AIChE J*. 2004;50:2526–2540.

6. Clayton R, Harold MP, Balakotaiah V. NOx storage and reduction with H_2 on Pt/BaO/Al_2O_3 monolith: Spatio-temporal resolution of product distribution. *Appl Catal B Environ.* 2008;84:616–630.
7. Olsson L, Persson H, Fridell E, Skoglundh M, Andersson B. A kinetic study of NO oxidation and NOx storage on Pt/Al_2O_3 and Pt/BaO/Al_2O_3. *J Phys Chem B*. 2001;105: 6895–6906.
8. Olsson L, Westerberg B, Persson H, Fridell E, Skoglundh M, Andersson B. A kinetic study of oxygen adsorption/desorption and NO oxidation over Pt/Al_2O_3 catalysts. *J Phys Chem B*. 1999;103: 10433–10439.
9. Bhatia D, McCabe RW, Harold MP, Balakotaiah V. Experimental and kinetic study of NO oxidation on model Pt catalysts. *J Catal.* 2009;266:106–119.
10. Bhatia D, Clayton RD, Harold MP, Balakotaiah V. A global kinetic model for NOx storage and reduction on Pt/BaO/Al_2O_3 monolithic catalysts. *Catal Today*. 2009;147S:S250–S256.
11. Xu J., Harold MP, Balakotaiah V. Modeling of the effects of Pt loading on NOx storage on Pt/BaO/Al_2O_3 catalysts. *Appl Catal B Environ.* 2011;104:305–315.
12. Cumaranatunge L, Mulla S, Yezerets A, Currier NW, Delgass WN, Ribeiro FH. Ammonia is a hydrogen carrier in the regeneration of Pt/BaO/Al_2O_3 NOx traps with H_2. *J Catal*. 2007;246:29–34.
13. Xu J, Clayton R, Balakotaiah V, Harold MP. Experimental and microkinetic modeling of steady-state NO reduction by H_2 on Pt/BaO/Al_2O_3 monolith catalysts. *Appl Catal B Environ*. 2008;77:395–408.
14. Xu J, Harold MP, Balakotaiah V. Microkinetic modeling of steady-state NO/H_2/O_2 on Pt/BaO/Al_2O_3 NOx storage and reduction monolith catalysts. *Appl Catal B Environ*. 2009;89:73–86.
15. Kabin KS, Khanna P, Muncrief RL, Medhekar V, Harold MP. Monolith and TAP reactor of NOx storage on Pt/BaO/Al_2O_3: Elucidating the mechanistic pathways and roles of Pt. *Catal Today*. 2006; 114:72–85.
16. Ohtsuka,H. The selective catalytic reduction of nitrogen oxides by methane on noble metal-loaded sulfated zirconia. *Appl Catal B Environ.* 2001;33:325–333.
17. Salasc S, Skoglundh M, Fridell E. A comparison between Pt and Pd in NOx storage catalysts. *Appl Catal B Environ.* 2002;36:145–160.
18. Amberntsson A, Fridell E, Skoglundh M. Influence of platinum and rhodium composition on the NOx storage and sulphur tolerance of a barium based NOx storage catalyst. *Appl Catal B Environ.* 2003;46: 429–439.
19. Benard S, Retailleau L, Gaillard F, Vernoux P, Giroir-Fendler. Supported platinum catalysts for nitrogen oxide sensors. *Appl Catal B Environ.* 2005;55:11–21.
20. Mulla SS, Chen N, Cumaranatunge L, Delgass WN, Epling WS, Ribeiro FH. Effect of potassium and water vapor on the catalytic reaction of nitric oxide and dioxygen over platinum. *Catal Today*. 2006;114:57–63.
21. Sharma M, Clayton R, Harold MP, Balacotaiah V. Multiplicity in lean NOx traps. *Chem Eng Sci*. 2007;62:5176–5181.
22. Sharma M, Haroldand MP, Balakotaiah V. Analysis of periodic storage and reduction of NOx in catalytic monoliths. *Ind Eng Chem Res*. 2005;44:6264–6277.
23. Balakotaiah V, West DH. Shape normalization and analysis of the mass transfer controlled regime in catalytic monoliths. *Chem Eng Sci*. 2002;57:1269–1286.
24. Burch R, Breen JP, Meunier FC. A review of the selective reduction of NOx with hydrocarbon under lean-burn conditions with non-zeoliteic oxide and platinum group metal catalysts. *Appl Catal B Environ*. 2002;39:283–303.
25. Scholz CML, Nauta KM, Croon MHJM, Schouten JC. Kinetic modeling of NO_x storage and reduction with different reducing agents (CO, H_2, and C_2H_4) on a Pt-Ba/γ-Al_2O_3 catalyst in the presence of CO_2 and H_2O. *Chem Eng Sci*. 2008;63:2843–2855.
26. Yi CW, Kwak JH, Janos S. Interaction of NO_2 with BaO: From Cooperative adsorption to $Ba(NO_3)_2$ formation. *J Phys Chem C*. 2007;111:15299–15305.
27. Balakotaiah V, Gupta N, West DH. A simplified model for analyzing catalytic reactions in short monoliths. *Chem Eng Sci*. 2000;55:5367–5383.
28. Hauptmann W, Votsmeier M, Gieshoff J, Drochner A, Vogel H. Inverse hysteresis during the NO oxidation on Pt under lean conditions. *Appl Catal B Environ*. 2009;93:22–29.
29. Fogler HS. *Elements of Chemical Reaction Engineering*. 4th ed. New York: Prentice Hall Professional Technical Reference; 2006.
30. Lesley MW, Schmidt LD, The nitric oxide + carbon monoxide reaction on platinum(100*). Surf Sci*. 1985;155:215–240.
31. Fissore D, Penciu OM, Barresi AA. SCR of NO*x* in loop reactors: Asymptotic model and bifurcational analysis. *Chem Eng J*. 2006; 122:175–182.
32. Allgower EL, Georg K. Introduction to numerical continuation methods. *Soc Ind Appl Math*. 1987.

Appendix : A Simplified Pseudo Arc Length Method that does not Involve Jacobian Matrix

This study involves the parameter dependent solutions to a set of nonlinear equations that can be generalized as

$$\underline{f}(\underline{x},\alpha)=0 \tag{A1}$$

where $\underline{f}$ and $\underline{x}$ are function and unknown vectors of dimension N, and α is the independent variable. Since α is also variable, Eq. A1 can be seen as N equations for $(N+1)$ unknowns with infinite number of solutions forming a curve in an $(N+1)$-dimensional space. For a typical chemical reactor model consisting of conservation equations with Arrhenius temperature-dependent parameters, all functions in $\underline{f}$ are smooth and differentiable with respect to both $\underline{x}$ and α. In this case, numerical continuation methods using predictor-corrector (PC) technique[32] can be used to trace the full solution curve, including the unstable branches that are otherwise difficult to find. Eq. A1 can be rewritten as

$$\underline{f}\left(\underline{y}(s)\right)=0 \tag{A2}$$

where $\underline{y}(s)=\left(\underline{x}(s)\alpha(s)\right)$ and s is the pseudo-arclength along the solution curve.

Since Eq. A2 contains $(N+1)$ unknowns and N functions with s as the independent variable, in order to solve the problem, an additional equation is required to complete the system as well as to define s. A commonly used equation for these purposes is

$$\sum_{I=1}^{N+1}\left(\frac{dy_I}{ds}\right)^2-1=0 \tag{A3}$$

where I is the index of unknowns. Taking derivative with respect to s on both sides of Eq. A2 gives

$$\frac{\partial \underline{f}}{\partial \underline{y}}\cdot\frac{d\underline{y}}{ds}=\underline{0} \tag{A4}$$

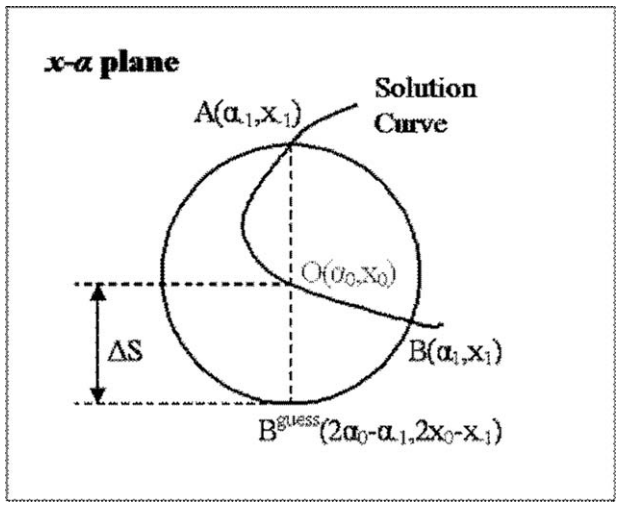

Figure A1. Schematic diagram of the continuation of simplified pseudo-arclength method for the case of scalar *x*.

where $\frac{\partial f}{\partial \underline{y}}$ is an $N \times (N+1)$ Jacobian matrix. As such, the nonlinear equation system defined in Eq. A1 can be converted to an initial value problem (IVP) defined by Eqs. A3 and A4. In practice, the IVP system is first stepwisely integrated as a "predictor" to provide a coarse estimate of the next point on the solution curve. Then with this estimate as the initial guess, Eq. A2 is locally solved as a "corrector" to polish the solution to a preset error tolerance.[32]

Typical implementations of PC continuation methods involve Jacobian matrix evaluation for the use of both predictor and corrector.[32] When the catalytic reaction system is described by a microkinetic model that is intrinsically complicated and open to continuous updates with surface species and reaction steps according to the latest research findings, the derivative evaluation may be tedious and human error prone. Herein, we present a simplified pseudo-arclength method that does not require explicit derivative evaluation.

Instead of Eq. A3, the additional equation to complete the system is given as

$$\sum_{I=1}^{N+1} \left(y_{I,J+1} - y_{I,J}\right)^2 = \left(s_{J+1} - s_J\right)^2 = \Delta s^2 \tag{A5}$$

where J is the index of solution point, Δs^2 is a preset parameter. Equations A1 and A5 form an $(N+1)$-dimensional nonlinear system that can be used to simultaneously solve and α, totally $(N+1)$ variables. The continuation along the solution curve is demonstrated in Figure A1 for the case of scalar x $\underline{y} = (x, \alpha)^T$. Equation A5 defines a circle on the x-α plane as shown in the figure. The circle center, point $O(x_0, \alpha_0)$, is the current solution point. The circle radius is the linear distance between two consecutive solution points, i.e.

$$\Delta s = \|A - O\| \tag{A6}$$

where $A(x_{-1}, \alpha_{-1})$ is the previous solution point. If Δs is of a proper value, the solution curve crosses the circle at another point different than A, giving the next solution point $B(x_1,\alpha_1)$. The prediction of B is given as point B^{guess} with $x_1{}^{\text{guess}} = 2x_0 - x_{-1}$ and $\alpha_1{}^{\text{guess}} = 2\alpha_0 - \alpha_{-1}$, or in the general vector form

$$\underline{y}_{J+1}^{\text{guess}} = 2\underline{y}_J - \underline{y}_{J-1} \tag{A7}$$

Noted is that, when $\underline{x}$ is an n-dimensional unknown vector, the circle in Figure A1 becomes an $(N+1)$-dimensional sphere. Among all points satisfying Eq. A5 and located on the sphere surface, the one defined by $\underline{y}_{J+1}^{\text{guess}}$ has the longest distance from the previous solution point defined by $\underline{y}_{J-1}$. It should be also mentioned that Eq. A5 reduces to Eq A3 as $\Delta s \to 0$. The predictor of Eq. A7, is, therefore, equivalent to a first-order approximation for integrating the aforementioned IVP system defined by Eqs. A3 and A4. Given by $\underline{y}_{J+1}^{\text{guess}}$ as the initial guess, a robust nonlinear solver that does not require explicit Jacobian matrix as the external input is needed to solve Eqs. A2 and A5. Fortunately, such solvers have been well established. DNEQNF package provided in IMSL FORTRAN library was directly used in this study.

Manuscript received May 21, 2013, revision received Aug. 19, 2013, and final revision received Oct. 12, 2013.